A&A 389, 271–285 (2002)
DOI: 10.1051/0004-6361:20020455

Astronomy & Astrophysics

HST observations of the protoplanetary nebula OH 231.8+4.2: The structure of the jets and shocks

V. Bujarrabal[1], J. Alcolea[2], C. Sánchez Contreras[3], and R. Sahai[3]

[1] Observatorio Astronómico Nacional, Apartado 1143, 28800 Alcalá de Henares, Spain
[2] Observatorio Astronómico Nacional, C/Alfonso XII, 3, 28014 Madrid, Spain
e-mail: j.alcolea@oan.es
[3] Jet Propulsion Laboratory, 4800 Oak Grove Drive, Pasadena CA 91109, USA
e-mail: sanchez@eclipse.jpl.nasa.gov;sahai@bb8.jpl.nasa.gov

Received 19 June 2001 / Accepted 21 March 2002

Abstract. We present high-resolution images obtained with the WFPC2, on board the *HST*, of the protoplanetary nebula (PPN) OH 231.8+4.2. Hα and NII line emission and scattered light in the continuum at 6750 and 7910 Å were observed. We also discuss NIR NICMOS images from the *HST* archive. The images show with high accuracy the shape and excitation state of the shocks developed in the nebula. Our high-resolution images (and data from other works) allow a very detailed and quantitative description of the different nebular components and of the physical conditions in them. We interpret specific structures identified in our images using existing models of shock interaction. In the center of the nebula, there is a dense torus- or disk-like condensation continued by an hourglass-like structure, with relatively high densities ($\sim10^5$–10^6 cm^{-3}) and temperatures ($\sim$30 K). Inside this torus we have identified the location of the central star, from SiO maser observations. Two shock regions are detected from the optical line emission images, respectively in the north and south lobes. In both regions, a forward and a backward shock are identified. The densities of this hot gas vary between 40 and 250 cm^{-3}, with the densest clumps being placed in the reverse shocks. The total mass of the shocked hot gas is $\sim2\times10^{-3}$ $M_\odot$, both lobes showing similar masses in spite of their different extents. The relatively collimated jet that impinges on an originally slow shell, so producing the shocks, is identified from the scattered light images and in CO maps. This flow is significantly denser and cooler than the shocked Hα regions. Its density decreases with the distance to the star, with typical values $\sim10^5$–10^4 cm^{-3}, and its temperature ranges between about 25 and 8 K. We explain the high Hα emission of the backward shock assuming that it propagates in a diffuse gas component, entrained by the observed collimated flow and sharing its axial movement. The existence of shocks also in the collimated densest flow is suggested by the high abundance of some molecules like HCO$^+$ and its structure and kinematics in certain regions, but they are not seen in Hα emission, probably because of the absence of (well developed) hot components in this dense flow. We think that the exceptionally detailed and quantitative image derived for the wind interaction regions in OH 231.8+4.2 is a challenge to check and improve hydrodynamical models of wind interaction in PPNe.

Key words. stars: AGB and post-AGB – stars: circumstellar matter – radio-lines: stars – planetary nebulae: individual: OH 231.8+4.2

1. Introduction

OH 231.8+4.2 is a well known nebula associated with an evolved star, probably in the protoplanetary nebula (PPN) phase. It has been extensively observed in optical and IR imaging (Reipurth 1987; Kastner et al. 1998), optical spectroscopy (Cohen et al. 1985; Sánchez Contreras et al. 2000a), OH maser emission (Bowers & Morris 1984), and thermal molecular lines (Sánchez Contreras et al. 2000b; Alcolea et al. 2001). OH 231.8+4.2 is clearly bipolar, but, contrary to what happens in most PPNe, one of the lobes is about twice as extended as the other. Its images show a clear axis of symmetry, oriented in the sky at a position angle of about 21°. The inclination of the axis with respect to the plane of the sky is relatively well known, 35°, the north lobe being the closest to us (e.g. Kastner et al. 1992). The distance to OH 231.8+4.2 is also well studied, $\sim$1500 pc (Bowers & Morris 1984; Kastner et al.), the corresponding total luminosity being $\sim10^4$ $L_\odot$.

The evolutionary status of OH 231.8+4.2 is still controversial. The central star shows a late spectral type,

Send offprint requests to: V. Bujarrabal,
e-mail: bujarrabal@oan.es

M9 III (Cohen 1981), and a long-period variability similar to those of AGB stars, though the nebula is similar to well known protoplanetary nebulae (PPNe) and very different from typical envelopes around AGB stars. Following the discussion by Alcolea et al. (2001), we will adopt that OH 231.8+4.2 is a PPN, while the stellar component may be peculiar or following an unexpected evolutionary path.

OH 231.8+4.2 belongs to the open cluster NGC 2437 (M 46). This situation has helped to estimate the distance to the object and its initial mass, which is thought to be $\sim$3 $M_\odot$ (Jura & Morris 1985; Alcolea et al. 2001).

OH 231.8+4.2 emits in Hα and optical forbidden lines, which show the existence of shocked material in a wide double-bubble. In the optical and NIR continuum, the image of the nebula, due to scattering by dust grains, is however narrow and elongated along its symmetry axis. The same narrow component is observed in CO line emission. The whole nebula is very extended, occupying more than 10^{18} cm. From the CO data it is possible to show that the temperature of the molecular gas is $\sim$10–30 K. This axially confined, cold gas is found to be very dense, representing most of the nebular material, $\sim$1 $M_\odot$. Meanwhile, the Hα emitting gas is hot, with typical temperatures $\sim$10 000 K, but just contains $\sim 10^{-3}$ $M_\odot$ (Alcolea et al. 2001; Sánchez Contreras et al. 2000a).

The kinematics of the molecular gas is remarkable. Its velocity shows a dominant axial component, which linearly increases with the distance to the star and reaches values as high as 430 km s^{-1}. The velocity of the Hα emitting gas also increases with the distance, reaching values similar to those of the cold gas, but also presents a component perpendicular to the axis, which is presumably responsible for its rounded shape. The CO data indicates that the expansion of the dense flow started about 800 yr ago. However, the kinematical age of the southern bubble is somewhat lower, $\sim$500 yr. We interpret (Sánchez Contreras et al. 2000a) that the dense molecular component was first accelerated by a strongly radiative shock (which explains its elongated shape), entering soon in interaction with more diffuse, outer shells. The expansion of the Hα rounded shell started as the result of the an adiabatic shock, produced when the cooling rate in the recently shocked region was low enough to allow the transition into the adiabatic regime.

To better understand the properties of both the shocked (Hα emitting) gas and the massive cool material (traced by dust scattering), we have performed very accurate imaging in optical line emission and continuum scattered light using the *HST*. We present here these data and a discussion on the general structure and dynamics of OH 231.8+4.2.

2. Observations

We have conducted observations of OH 231.8+4.2 using the Wide Field and Planetary Camera 2 (WFPC2), on board the *HST*. The nebula was placed in the WF3 chip, which has a pixel size of $\sim$0.1 arcsec, about twice as large as the nominal telescope spatial resolution. We obtained images using the narrow filters F656N and F658N, that accurately isolate the emission of the Hα and NII 6580 Å lines, respectively (mean wavelengths: 6563.9 and 6590.1 Å, effective widths: 21.4 and 28.5 Å, respectively; see the WFPC2 Handbook). We also observed with the wide filters F675W and F791W, which probe the emission around, respectively, 6750 and 7910 Å (mean wavelengths: 6695.9 and 7826.3 Å, effective widths: 865.6 and 1205.0 Å, respectively). A total of seven orbits were required to perform our observations, since long exposures were necessary due to the low surface brightness of the source. The analysis was done following the prescriptions given in the *HST Data Handbook* and using the usual tasks in IRAF (including the "stsdas" package).

The combination of the images was performed using the "stsdas" task "gcombine"; we have checked that it reasonably eliminates cosmic rays without introducing spurious effects on the source intensity or background noise. At least three individual images with different exposure times were obtained for each filter, seven exposures were obtained with the F656N one. The effects of the introduction of different exposures in the combination procedure were carefully checked, particularly on the signal and noise levels; no saturation was found in the nebular images (as expected for its low brightness). Further cosmic ray rejection was performed using the task "cosmicrays", in the "noao" package; again we have checked that the task acts only on cosmic rays, not on background stars, noise, nebular structure, etc. Due to the long exposures used (up to 2700 s with F656N) and the high number of stars in the field (our source is in a star cluster, see Sect. 1), the cosmic ray effects and field star images significantly affected the individual exposures. We think that they were appropriately treated in the final images.

Astrometry was performed by means of the "stsdas" task "metric", which takes into account projection effects and the chip deformations, and taking into account the known coordinates of reference stars in the field. Accurate astrometry is necessary in our case, since we will compare our images with high resolution maps obtained from radiointerferometers (for which an absolute position accuracy $\sim$0.″1 is expected).

The *HST* Handbook states that the pointing uncertainties and possible errors in the guide star positions lead to uncertainties in the image absolute coordinates of about 0.5 arcsec. The relative coordinates are expected to be much more accurate. We have calculated the relative positions of different stars (of the many ones present in the field), for the different images over the seven orbits and three different visits; a total of 8 stars in the WF3 field were used for such a purpose. For observations with the same filter, the measured shifts were always smaller than 0.5 pixel, so no corrections were applied when combining the different exposures (which would had introduced a lost of the sharpness in the resulting images and a spuriously low noise level). However, larger corrections were found between observations with different filters; such shifts were

as large as 1 pixel between the F675W and the F656N images and clearly noticeable if image differences are performed without any correction. For that reason, in order to estimate the pure line emission image, we have shifted by the appropriate values the F675W image before subtraction. However, the final images of the different filters were not shifted, to avoid loss of image quality; instead, we have changed the conversion of pixel number to coordinates to yield all images in J2000 coordinates.

To determine the absolute (FK5) coordinates in our images, we have compared the results provided by "metric" with stellar positions in the *HST* Guide Star Catalog, version 2.2. We have taken into account 28 stars in the three WF chips that are listed in this catalog. We have also checked that the coordinates of stars in both the GSC2 and Hipparcos catalogs at less than 2′ from our object are coincident between 0.″1. Comparing the nominal positions of these stars and those obtained from the images, systematic shifts are found. We found a shift in right ascension $\sim -0.6 \pm 0.2$ arcsec and a shift in declination $\sim -0.5 \pm 0.2$ arcsec (measured − nominal coordinates). We corrected these shifts in the global conversion from pixels to J2000 coordinates.

The effects of the geometric distortion introduced by the telescope optics, calculated by means of the "stsdas" task "metric", and the absolute astrometric corrections mentioned above of the field, are taken into account in all our images. The best coordinate measurements can only be represented by means of (curved) lines of constant right ascension and declination; see Fig. 1. In any case, we must keep in mind the expected uncertainties in the absolute positioning mentioned above. The image coordinates resulting from doing this correction allow a reasonable comparison with radio data (Sect. 3). We have plotted on our images the expected position of the central star, as measured from observations of SiO maser emission (see Sánchez Contreras et al. 2000b and Sect. 3.3).

Calibration from the pixel count number to physical units was made using the PHOTFLAM parameter (see the *HST data Handbook* and *WFPC2 Handbook*). Such a procedure is thought to be accurate to a few percent. Such an accuracy is largely enough for all possible comparison with other optical data, a very difficult task due to uncertainties in the calibration of images taken from the ground and, mainly, to the different telescope characteristics; not to speak of the comparison with theoretical predictions. All our maps are calibrated in units of erg cm^{-2} s^{-1} $\mathrm{Å}^{-1}$ (per pixel).

As we have mentioned, the F675W image was used to subtract the contribution of the continuum to the Hα and NII line images. Even if the characteristic wavelength of this channel was very similar to those of the line filters, the very red continuum of the nebula made it necessary to introduce some correction to the continuum image. From the large intensity ratio between the F791W and F675W images we can estimate that the correction to F675W, when used to be subtracted from the F656N image, is as large as 40%. However, the very accurate factor needed for the subtraction had to be calculated by estimating the ratio between the intensity in the strong continuum regions in both F675W and the line filters (reasonable factors were obtained). Note that we fortunately know from spectroscopic data (Sánchez Contreras et al. 2000a) that the line emission in these regions is negligible. Even doing so, the large differences in the obscuration that exist between different points in the continuum image lead to an imperfect continuum subtraction, residuals can be seen in the pure line images by careful inspection. The resulting continuum subtracted images of Hα and NII 6580 Å line emission are presented in Fig. 1. The continuum images at 6750 and 7910 Å are also shown in Fig. 1.

In order to obtain color images some extra manipulations are needed. First, it is necessary to accurately eliminate as far as possible the residual flux level detected in points out of the nebula, ∼3 counts in the combined continuum images (not much smaller than the emission in the weaker regions). Second, it is possible to identify the contribution in the F675W image of contamination by atomic line emission (Hα, NII, OI and SII are likely contributing in the strong northern shocks). We tried to subtract this line contamination by estimating a scaling factor to be applied to the Hα image; this factor was estimated from examining the intensity in the F675W of regions in which the F791W is negligible but the Hα line is strong. To decrease the effect of such a correction on the true continuum emission, we used in fact the continuum subtracted Hα image as reference. We have checked that the correction is only noticeable in the northern double shock and is smaller than 1% in the regions in which the continuum is dominant. The image shifts are also taken into account. After these image treatments, the ratio between the calibrated continuum images at 7910 and 6750 Å was calculated, see Fig. 2. (We recall that, because of the slight influence of the line contamination on the 6750 Å image and the difficult estimation of the correction factors used above, we show in Fig. 1 the F675W images without any line image subtraction.)

2.1. NIR NICMOS data from the HST archive

We have also used in our analysis NIR images obtained with the NICMOS camera on board the *HST*. These data were obtained from the *HST* archive (*HST* Proposal 7365, by William Latter et al.; see also Bieging et al. 2000). From that project, we have only used the images of the nebular continuum emission in the H and K band, taken with the NICMOS2 camera using the filters F160W and F205W, whose central wavelengths (and equivalent widths) are respectively 16 060 Å (1177 Å) and 20 714 Å (1832 Å); see the *HST Data Handbook* for more details. The results, H band and $[H-K]$ color images are presented in Fig. 3.

Data reduction was also performed using the "stsdas" package in IRAF. Cosmic ray and hot pixel removal was done by comparing the two exposures available for each

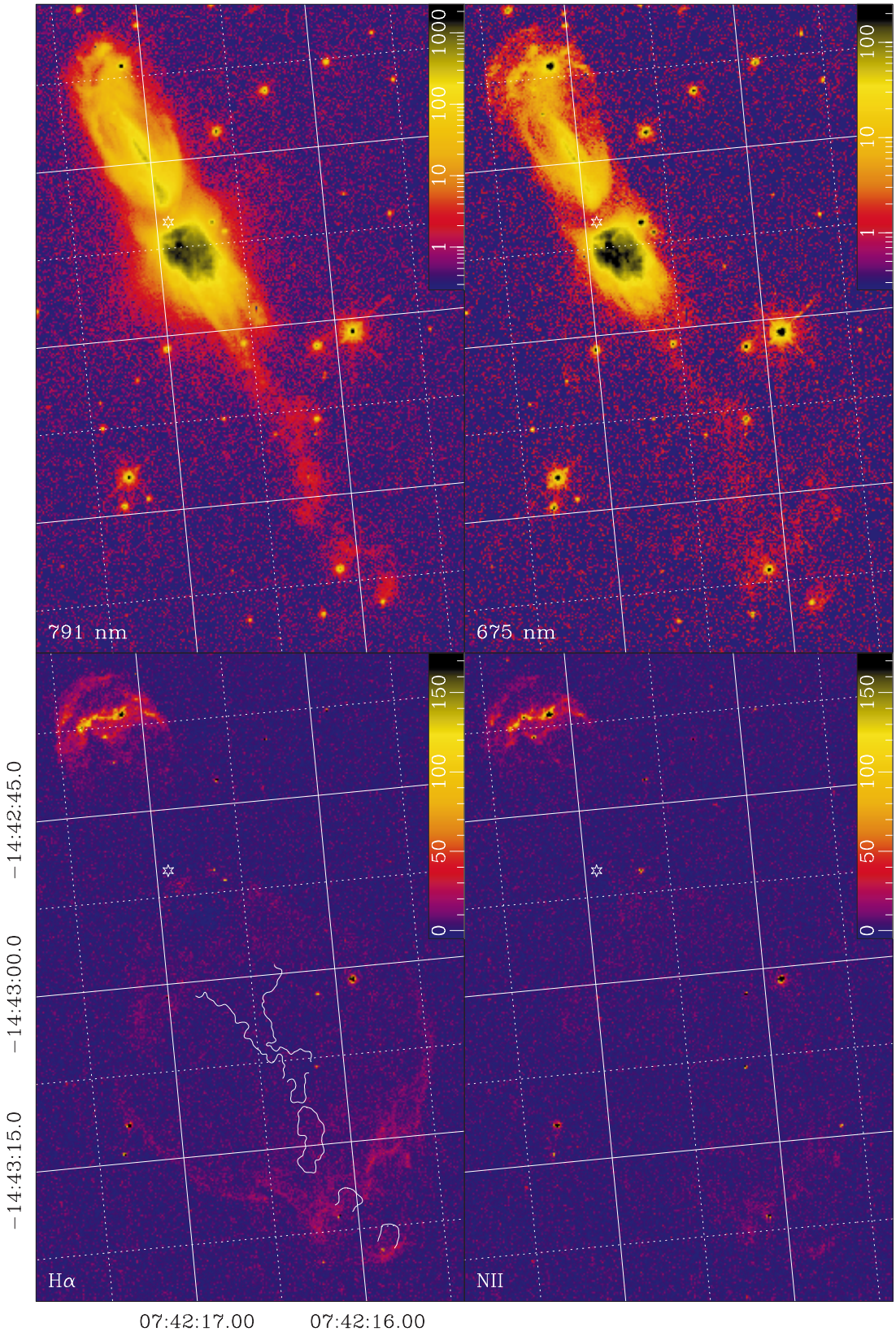

Fig. 1. Images in OH 231.8+4.2 of the continuum at 7910 and 6750 Å and of Hα and NII pure line emission (after subtraction of the continuum contamination in these filters). No subtraction of line emission within the continuum filter bandwidths is done. The expected position of the central star is indicated by an asterisk (see text). Color bars indicate the conversion from the false color scale to physical units, 10^{-20} erg cm^{-2} s^{-1} Å^{-1} (per pixel). The white contour in the Hα image represents the southern features in the 7910 Å image.

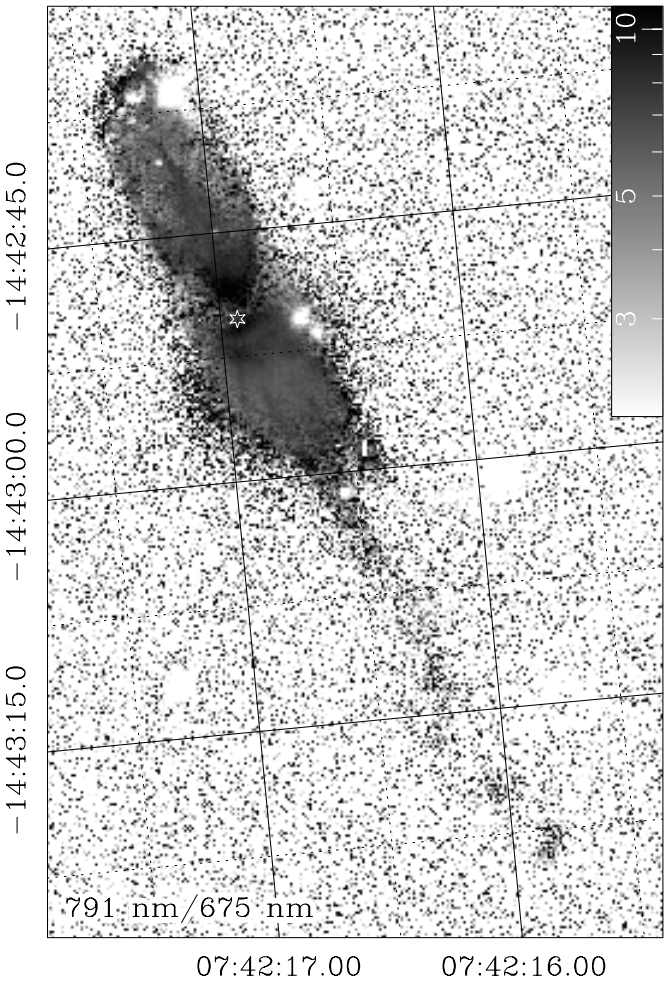

Fig. 2. *HST* WFPC2 image of the 7910 Å/6750 Å intensity ratio in OH 231.8+4.2. See Fig. 1 and Sect. 2 for the meaning of symbols and data analysis.

filter. Shifts in position between all exposures were measured by using several stars in the field. These shifts were corrected before averaging the images of the same band and before computing the $[H-K]$ color image. To compute this color image, elimination of the residual background level was also performed. This removal can not be done very accurately since, due to residuals in the flat field subtraction, the zero level is not the same through the full images (see e.g. the low level emission to the west of the nebula in the H band image). Due to this, for regions of low level emission, the image ratio has no sense; we have masked out these areas in the $[H-K]$ color image shown in Fig. 3. The data were finally calibrated in units of $10^{-20}\,\mathrm{erg\,cm^{-2}\,s^{-1}\,\AA^{-1}}$ (per pixel) using the value of the parameter PHOTFLAM in the *HST* data headers.

Since we are mainly interested in comparing these NIR images with those taken by us with the WFPC2, we have re-sampled the NICMOS data so they are, on a pixel by pixel basis, directly comparable to the WFPC2 ones. This means that we have not only rotated and shifted the NICMOS images, but also we have re-sampled them, taking into account both the larger pixel size of the WF3 chip of the WFPC2, and the geometric distortions present in this camera (and not in NICMOS2). Obviously, in this process we have lost some spatial resolution. The absolute coordinates for the NICMOS2 images were determined by comparing the position of the field stars present in both NIR and optical images (we have already described how we determined the absolute position of the WFPC2 images).

3. Results

In this section we will discuss the different components that can be identified in our WFPC2 images. In particular, we will compare them with the NIR images (Sect. 2.1) and the CO $J=1$–0 and 2–1 emission maps, from Alcolea et al. (2001). In Fig. 1 we can see the general structure of the nebula from our *HST* imaging.

Hα and NII (6583 Å) optical line emissions are known to be good tracers of shocks, particularly in this nebula, in which the central star is too cool to ionize the surrounding material (e.g. Sánchez Contreras et al. 2000a). However, the intensity of the light scattered by nebular dust is independent of excitation conditions, and is therefore a good tracer of the density distribution, except in regions of high optical depth. Indeed, we find that our scattered light images are very similar to the cold gas distribution measured by means of CO mm-wave emission (Alcolea et al. 2001, see also Sect. 1), except in the highly obscured equatorial regions. This dependence on the physical conditions is confirmed by estimations from our data (see Sect. 4): the gas traced by CO is cold (with kinetic temperatures T_k ∼10–30 K) and shows typical densities, n, between 10^4 and 10^6 cm^{-3}, while in the shocked gas emitting in Hα T_k ∼10 000 K and n is always $<10^3$ cm^{-3}. As we have mentioned, Sect. 1, both mm-wave and optical spectroscopy also show that both the axially confined cold component and the inflated hot lobes lobes flow at similar, very high outward velocities.

Our continuum images therefore trace the densest and coldest regions within the lobes of the nebula, which constitute a relatively collimated high-velocity outflow. The optical line images show wide inflated lobes with high velocity and excitation, which are the result of shocks. This configuration suggests that the shocked gas is the result of the interaction of the collimated outflow with a less dense shell, which was originally flowing at a smaller velocity. As we will see in the next subsections, this interpretation is confirmed by a more detailed analysis of our observations. In the center of the nebula, there is a high-obscuration, torus-like region that hides the central star both in optical and NIR bands.

3.1. The northern shocked region and axial dense flow

In Fig. 3 (bottom panels) we show enlarged images of the northern lobe in 7910 Å continuum and pure Hα and NII line emission (after subtraction of the continuum contribution, see Sect. 2).

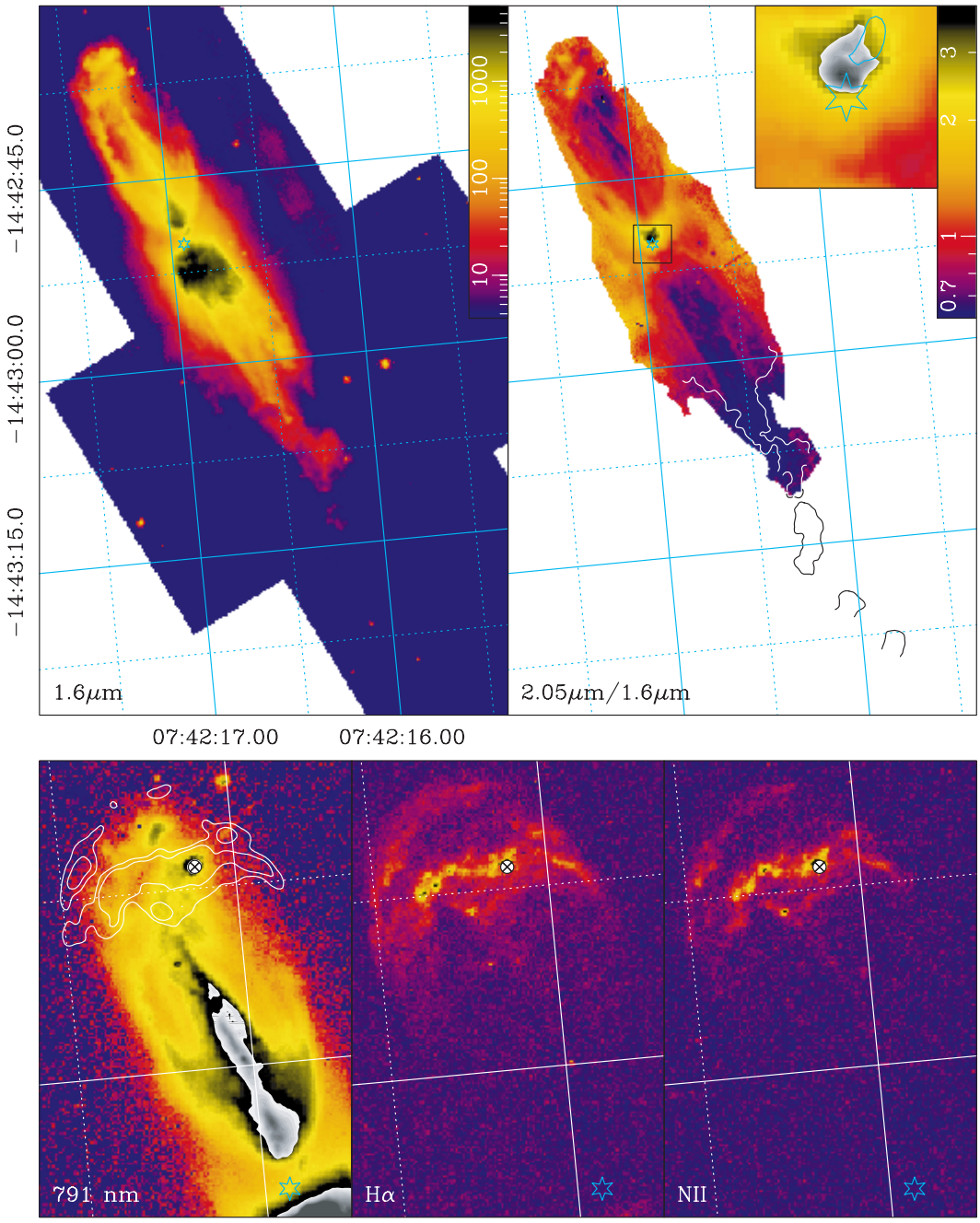

Fig. 3. Top: images of OH 231.8+4.2 in NIR continuum at 1.6 μm (H) and $[H-K]$ color (2.05 μm/1.6 μm intensity ratio), from *HST* NICMOS2 imaging. Units are 10^{-20} erg cm^{-2} s^{-1} Å^{-1} (per pixel). As for Fig. 1, the contour in the $[H-K]$ image represents the southern features in the 7910 Å image. The inset reproduces the 3″-wide region around the star; the asterisk shows the star's position and its uncertainty (with respect to the $[H-K]$ image) and the blue contour represents a relative elongated maximum in the H image. Bottom: enlarged *HST* images of the northern lobe in 7910 Å continuum, Hα emission and NII emission (see Fig. 1). The white contour on the enlarged 7910 Å image represents the Hα emitting regions. A strong field star has been crossed out in the lower panels.

3.1.1. The structure of the shocks

Our Hα and NII images of the northern lobe show the presence of a double shock. First, a bow-like feature is located at the end of the lobe (labeled A in Fig. 4). There is a second feature that is somewhat closer to the star and roughly perpendicular to the nebular axis (feature B_2, and its wide counterpart B_1). The maximum emission in this feature is coincident with a minimum in the continuum images. We also note that the bow shock appears just beyond the end of the narrow lobe detected in both CO and scattered light and that both shock features are significantly more extended, perpendicularly to the direction of the axis, than the dense axial flow, which is just 2–3″ wide. Finally we note that there is a clear maximum of the scattered light image (feature F in Fig. 4) almost

exactly in the middle of the two line emission features. In this sense, the images of the line emission and scattered light in the northern lobe are almost complementary. We therefore conclude that the Hα and NII emitting gas is distinct from the dense axial flow, and confirm that the high-excitation shocks occur in regions where the density is relatively low. These conclusions are confirmed by calculations of the physical conditions derived from both Hα and CO emission, which yield significantly different values (Sect. 4) for both components, the Hα emitting gas being in particular significantly less dense. We note that projection effects could be responsible for some of the coincidence between the line and continuum brightness distributions that appear in our images.

As we have mentioned, a composite shock front is detected in our line emission images. The bow-like feature, located at the end of the lobe, very probably corresponds to the forward shock expected in the interaction of a collimated fast jet with a slow shell, because of both its location and shape. The inner line-emission feature (perpendicular to the axis) is however very different and we interpret it as coming from gas excited by the terminal jet shock, i.e. the shock propagating backward in the jet that decelerates it close to the interface with the slow shell. The discontinuity in physical conditions associated with such shocked gas is identified with the Mach disk. Note that in this region, the shocked gas must be redirected outward from the axis, due to the increase of the pressure of the jet gas.

The best theoretical descriptions of such shocks are probably those by Frank & Mellema (1996), Raga et al. (1995) and Stone & Norman (1993a,b). See in the calculations by Frank & Mellema (their Fig. 3) the features at 1.3–1.5$\times10^{17}$ cm. Note in particular the predicted shape of the gas heated by the terminal jet shock, very similar to the observed feature. In the models by Frank & Mellema (1996), however, the fast jet is assumed to be diffuse (whereas the axial flow in OH 231.8+4.2 is dense), which must be taken into account when comparing these theoretical results with our observations. In the calculations by Raga et al. and by Stone & Norman, in which the jet is denser than the shell (probably more in agreement with our case), the shape of the Mach disk and associated shocked gas is also similar to the observed inner feature. But, when the jet is very dense, the predicted backward shocks are much less developed and cooler than the forward shock. Raga et al. (1995) indeed predict that the Hα emission associated with the Mach disk must be negligible compared to that of the forward shock.

In general, it is known that the shocks propagating in the denser component must always be less excited. This is because the energy won per unit mass after the shock must be lower for this dense component, and also to that the cooling rate rapidly increases with the density; see Hartigan et al. (1987), Raga et al. (1995), Frank & Mellema (1996), Mellema & Frank (1997), etc. Hartigan (1989) showed, for instance, that the Hα emission is similar in the Mach disk and forward shock only when the densities of both the slow shell and collimated jet are of the same order, the forward shock emission being more/less intense when the shell density is significantly lower/higher than that of the jet. Therefore, under quite general conditions, the shocks affecting the densest regions are the least excited ones. The shocks affecting the diffuse regions would be the strongest emitters in optical lines, whereas the dense regions would lack such emission, even if there were shocks propagating in them (note that shocks propagating in dense gas can be identified by other means, see Sect. 3.1.2).

This dependence of the optical line emission on the density explains the lack of correlation found between the distribution of the dense gas and the Hα and NII images. But it seems in contradiction with the detection in our source of optical lines from the backward shock, since the collimated flow is dense. We think that this contradiction is only apparent: The inner Hα feature (B_2 in Fig. 4), which is distinct from the dense gas detected in scattered light and CO emission, would correspond to the part of the backward shock propagating in the relatively less dense components of the fast flow (perhaps entrained in some way by the very dense gas). The required density variations could be due to a density decrease outward from the axis in the collimated fast flow or to density variations along the axis. The latter case would be similar to the "pulsed" jet studied by Stone & Norman (1993b). As we can see in their Figs. 1 and 3, the highest ionization fraction systematically appear anticorrelated to the dense "pulses": the high ionization (i.e. the high excitation and probable Hα emission) appears in the low-density regions that are distributed along the axis, alternating with high-density (low-excitation) clumps. In any case, the theoretical description of backward shocks propagating in a jet with such complex density laws (and for the other conditions expected in PPNe) have been barely investigated to date and our conclusions at this respect are for the moment tentative.

An alternative explanation to the observed shock structure would be the presence of multiple or variable post-AGB ejections (in some way a limit case of the complex jet structure proposed above), producing a series of bow shocks. However, we think that our interpretation offers the simplest explanation for the observed structures and is supported by theoretical modeling.

The identification of the inner Hα feature in the northern lobe with the terminal backward shock, in principle based on the overall geometry, is supported by the following independent arguments. 1) The velocity field observed in Hα long-slit data (Sánchez Contreras et al. 2000a), including the variation of the mean value and dispersion of the radial velocity as a function of offset from the polar axis, can be explained by a lateral velocity component (i.e. movements perpendicular to the axis) in this region. 2) The observed value of the Hα/NII line intensity ratio is different for the backward and forward shocks in the northern lobe (in the reverse shock, it is quite constant and $\sim$1, in the outermost shocked regions the line

ratio can be larger than 5). Theoretical models predict that the NII (6583 Å) emission from shock-excited gas should require higher excitation, and therefore should be be more strongly dependent on the shock conditions, than the widespread Hα emission (see e.g. Hartigan et al. 1987, who found a significant increase of the NII predicted intensity for their models of high-velocity shocks, which was not the case of Hα). The observed variations in Hα/NII intensity ratio are then expected, since both shocks propagate in different media and will probably show different excitation states. 3) The peculiar continuum brightness distribution, molecular abundances and gas kinematics found in the region of the dense axial flow close to this Hα feature (Sect. 3.1.2) suggest that the shock acts on the axial flow (even if Hα is not intense in its densest component), as is the case for a reverse shock. 4) If the inner Hα feature represents the terminal backward shock, and under the interpretation of the thermodynamics of the shocks by Sánchez Contreras et al. (2000a), the distance between the backward and the (adiabatic) forward shocks must be similar to the cooling distance in the non-radiative regime. The measured distance, $\sim 10^{17}$ cm, is indeed comparable to expectations by Sánchez Contreras et al.

3.1.2. The dense collimated flow

In addition to the shock structures detected in the optical line images, we identify a very dense, axially confined component from our scattered light images (also seen in CO mapping, Alcolea et al. 2001, but with significantly lower resolution). The central part of the continuum northern lobe will be referred to as feature G (Fig. 4), and the outermost clumps correspond to feature F (note that features F to J in Fig. 4 in fact correspond to components detected in CO emission).

The role in the wind interaction of this axial feature is remarkable. The CO data show that the axial velocity of the dense gas in OH 231.8+4.2 increases linearly with the distance to the center (Alcolea et al. 2001). This ballistic velocity law is easily explained assuming that the gas was accelerated at the very beginning of the post-AGB phase and has continued freely flowing since then. This is not surprising, since such a very high mass cannot be strongly decelerated by the interaction with the much more diffuse outer gas (see Sects. 1 and 4).

On the other hand, it is likely that there are also shocks affecting the dense, axial component, even if they are not intense in optical lines. In the tip of the northern lobe, the above mentioned velocity/distance law seems to be altered, and apparently some deceleration of the gas is present (see Fig. 5 in Alcolea et al. 2001 and a detailed comparison between CO and *HST* data in Alcolea et al. 2002). In this region, the shocks have probably been able to modify also the structure of the dense jet, as shown by the significant brightness variations in our continuum images. It is also interesting to compare our optical imaging with the line emission of the HCO^+ molecule, which is expected to be detectable only from recently shocked (but already cooled down) gas, see Sánchez Contreras et al. (2000b). HCO^+ shows a remarkable maximum at east and north offsets from the central star of $+4\farcs5$ and $+11\farcs5$, respectively (also indicated in Fig. 4). This maximum is coincident with a region of the (Hα emitting) backward shock and with a dense region identified from the continuum images. Both the presence of intense HCO^+ emission and the peculiar kinematics and structure in this northernmost dense gas identify, in our opinion, shocks propagating in it.

Therefore, the dynamics and structure of the dense, collimated flow lead us to propose that, after impinging on a slow wind, it released the energy needed to form the high-temperature shocks detected in optical line emission. The backward shock detected in Hα is apparently distinct from the densest, collimated flow because, as we have mentioned, this Hα feature could come from a relatively more diffuse (and less axially confined) component of this collimated outflow. The relatively high excitation expected for this diffuse component should favor Hα and NII emission, while reverse shocks acting on the densest flow would only be detectable by other means.

Finally we note that the dense axial component seems to lie in the interior of an elongated cavity, whose limb-brightened appearance in the scattered light images suggests that it is bounded by geometrically thin walls. These walls can be identified in the CO maps (from Alcolea et al. 2001), which suggests a relatively low excitation (also note the lack of an Hα counterpart). The CO emission in most of this component is however weak, except in the region where the walls are very close to the axial flow, at $\lesssim 4''$ from the star. We suggest that the cavity has been formed by the passage of the shock fronts. Note that the walls are extended along the axis up to the region occupied by the reverse shock, but that the lateral extent of the cavity is significantly smaller than that of the shock fronts. This idea is compatible with the relation between the Hα feature perpendicular to the axis and a Mach disk, which is sending outwards from the axis some of the material of the collimated flow, of which the walls would be formed.

3.2. The southern Hα bubble and elongated scattered light component

3.2.1. The hot shocked gas

Our images of the southern lobe of OH 231.8+4.2 (Fig. 1) show that the collimated flow, probed by scattered light in the optical (and by CO line emission), and the hot bubble, probed by Hα and NII line emission, are clearly distinct components.

As we have mentioned, the regions observed in Hα emission in OH 231.8+4.2 are very probably excited by shocks, the temperature in such regions is $\sim$10 000 K, but densities are always smaller than 1000 cm^{-3} (Sánchez Contreras et al. 2000a, Sect. 4). In the southern lobe, there is a wide bubble detected in Hα and NII images

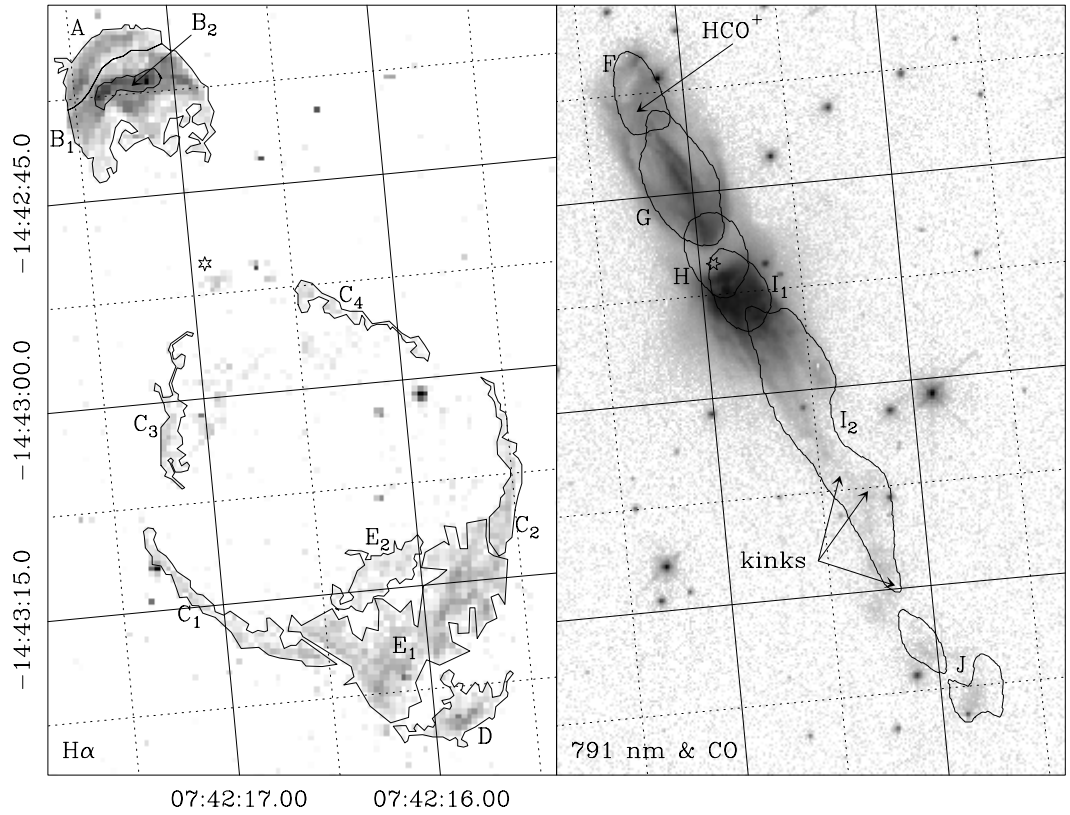

Fig. 4. Different components of OH 231.8+4.2. Left: Hα emitting lobes; the different polygons indicate the regions over which the Hα emission was integrated for calculating the emitting mass. Right: CO line emission components, contours (features F to J; from Alcolea et al. 2001), superposed on our scattered light image at 7910 Å, grey scale; note that there is a certain spatial overlap between the CO components because they were defined in that work by means of different velocity intervals. We also indicate the position of the northern HCO^+ maxima and the southern flow kinks. See Fig. 1 for more detailed images and Sect. 3 and Table 1 for a description of the features.

(feature C in Fig. 4). Excluding very small condensations (Sect. 4), the typical densities in the southern Hα emitting regions are $\sim$50 cm^{-3}. The bubble is known to be in expansion, both in the axial direction and perpendicularly to it, reaching velocities $\sim$400 km s^{-1} in the southernmost features (Sánchez Contreras et al.).

The end of the Hα bubble shows a complex structure. Another "dome" or "blister" appears at the very end of the lobe (feature D in Fig. 4). The intersection of both domes is a region of particularly intense emission in optical lines (feature E). The shape of the whole structure resembles that found in the northern lobe; but at a larger scale and with less sharp contours.

Following the reasoning given in Sect. 3.1, we think that the two domes (features C and D in Fig. 4) are a forward shock and that the impinging jet is the dense axial flow detected in scattered light. The intense line region at the dome intersection (feature E) could be due to the terminal jet shock or at least be associated with it. Although such an interpretation is clearly less well supported by observations than for the northern lobe, we will adopt it, following these arguments: 1) Analogy with the north lobe case, including some properties also discussed in that case (Sect. 3.1.1), like the relatively high NII intensity in the possible reverse shock and the remarkable fragmentation and sinousity shown by the collimated flow close to the dome intersection (Sect. 3.2.2). 2) The shape of the structure is more or less comparable to those predicted by models. Calculations by Frank & Mellema (1996) and Stone & Norman (1993a,b) show the presence of two domes; these calculations also show that the terminal backward shock (and the Mach disk) are connected to the dome intersection, through a shocked gas extension (however the model calculations by Raga et al. 1995, also mentioned in Sect. 3.1, do not show a behavior of this kind).

As for the northern shocks (Sect. 3.1.1), such a possible backward shock would not be acting on the very dense and collimated flow, but probably on diffuser gas (in some way entrained by it in the axial direction), since its extent perpendicularly to the axis is much larger than that of the dense flow. On the other hand, theory predicts that Hα emission, in general, does not come from the backward shocks propagating in the densest collimated flow, since the the hottest shock features tend to be those propagating in the most diffuse components (as we have already discussed in Sect. 3.1). As we have also mentioned, this does not mean that there are not shocks in the densest clumps, but the shocked dense gas would be cool and only detectable by means of other tracers.

3.2.2. The dense collimated flow

An elongated and much denser component (with densities between 10^5 and 4×10^3 cm^{-3}, see Sect. 4) is identified from our broad-band images, which show light scattered by dust grains, see features I, J in Fig. 4. This component coincides with the southern features seen in CO emission, but is not seen in optical line emission. In fact, it runs along the axis in the center of the southern Hα bubble. The molecular gas shows axial velocities of the same order of those of the Hα emitting gas; an almost constant velocity gradient along the axis is found, the highest velocities being placed at the tip of the lobe (Alcolea et al. 2001). But there are also deviations from this simple law. In two regions, between about 10″ and 18″ and between 23″ and 29″ from the central star, the velocity gradient is smaller than the average. In the intermediate region, the gradient has a value larger than the typical one. Precisely in this high-gradient region there is a significant change in the collimated flow direction (Figs. 1 and 4). This result can be explained assuming that the collimated flow kinks in such a way that changes in the orientation (with respect to the line of sight) induce changes in the radial velocity with respect to the observer. Of course, it is also possible that the observed changes correspond just to changes in velocity modulus. (A detailed deconvolution of the CO and long-slit optical observations to get, for possible velocity fields, three dimensional descriptions of the density and velocity distributions in the whole nebula is possible but very complex, and obviously out of the scope of this paper; see Alcolea et al. 2002.)

At the end of the lobe, at distances from the star farther than ∼26″, the collimated flow becomes fragmented in several condensations (feature J in Fig. 4).

We have suggested that the dense collimated flow acts as the jet that impinges on a slow diffuse shell, releasing the momentum needed to form the shocks detected in Hα, as for for the northern shocks (Sect. 3.1). Two of the arguments used in that case, the disruption of the dense collimated tail seen in CO and scattered visible light and the fact that it stops just behind the Hα forward shock, can be also applied to the southern regions. We stress the strikingly tight association between the last clump detected in the red continuum and the southernmost Hα feature: the scattered light feature is inwards than and clearly in contact with the Hα one, it is difficult to avoid the conclusion that the dense clump is literally pushing the Hα emitting gas.

3.3. The center of the nebula and the maximum of scattered light

Hα emission is very weak from the central parts of the nebula (see our continuum-subtracted images, Figs. 1 and 3, bottom, and spectroscopic data by Sánchez Contreras et al. 2000a), except for the southern lanes that appear in the images forming an angle ∼±40° with respect to the symmetry axis (a part of the wide bubble discussed in Sect. 3.2.1). In these inner regions, the continuum images, due to scattering by dust grains, show however rich intense features.

A disk- or torus-like high-obscuration region appears in the center. We have represented in our images by asterisks the position of the SiO maser, which is known with an accuracy better than ∼0.″1 from Plateau de Bure connected interferometry, Sánchez Contreras et al. (2000b) and VLBA long-baseline interferometry, Sánchez Contreras et al. (2002). In the latter paper, it is argued that the SiO maser structure is closely associated with the central M-type star, since the total extent of the maser emission is only slightly larger than the stellar size itself. So, this position can be used to identify the central star of OH 231.8+4.2; in fact the maser data are the most accurate way to locate the star in our case. The continuum light in the optical and NIR shows a relative minimum in this disk-like feature that surrounds the central star (Figs. 1, 3). We also note the presence of an elongated relative maximum at about 1″ from the star, represented by the blue contour in the inset in Fig. 3 (right-upper panel). The shape and position of this structure, clearly associated with a minimum in the 2.05 μm/1.6 μm intensity ratio, suggests that it corresponds to a region with relatively low obscuration or showing intense second order scattering, due to some fortunate geometrical coincidence. This interpretation is supported by the approximate coincidence of the assumed position of the star with the maximum of the obscuration seen in the optical and NIR color images (Fig. 3, top panels) and with the maximum of the CO emission at the systemic velocity (∼33 km s^{-1} LSR, Alcolea et al. 2001).

The fact that the central star is not detected to a limit $\sim 10^{-20}$ erg Å^{-1} cm^{-2} s^{-1} in our 7910 Å image, although its unabsorbed intensity per pixel should be $\sim 5\times10^{-12}$ erg Å^{-1} cm^{-2} s^{-1} (for a total luminosity $\sim 10^4$ $L_\odot$ and an efficient stellar temperature $T_{\rm eff} \sim$ 2500 K, see Sect. 1), shows that the obscuration is high. We deduce that the dust extinction at 7910 Å in this direction is $\gtrsim$22 mag. We estimate, from the standard conversion from optical extinction to gas column density in the interstellar medium, that more than about 5×10^{22} cm^{-2} particles are in front of the star. If the typical length of this column is 2.25×10^{16} cm (equivalent to 1″ in the images), we deduce in the central torus an average density $\gtrsim 2\times10^6$ cm^{-3}.

The absence of a stellar image in the NICMOS data also gives a limit to the optical depth in the NIR. We estimate that the stellar image in our *H*-band image (Fig. 3) is weaker than $\sim 20\times10^{-20}$ erg Å^{-1} cm^{-2} s^{-1} and that the expected stellar emission would be $\sim 6\times10^{-12}$ erg Å^{-1} cm^{-2} s^{-1}. So an extinction $\gtrsim$19 mag is expected at this wavelength, which, following the above reasoning, would yield column densities $\gtrsim 10^{23}$ cm^{-2} and densities $\gtrsim 5\times10^6$ cm^{-3}.

These values of the density are very high but expected, since the CO data indicate average densities in the inner ∼3″ of about 3×10^6 cm^{-3} (Alcolea et al. 2001). So, the

limits to the column density derived from the nondetection of the central star are compatible with the high densities expected in the central regions of OH 231.8+4.2.

The northern and southern nearby regions are however bright in scattered light. Obviously, these clumps reflect the stellar light that escapes by the polar holes of the central, opaque torus. The southern region is significantly brighter that the northern one, despite the north lobe is pointing to us (see comments in Alcolea et al. 2001). Both inner lobes are complex, with filaments close to the axis and a kind of hourglass structure. In general, CO emission also traces both the axial filaments and the hourglass structure (Alcolea et al. 2001; note that in this case the lower resolution of the CO data, $\sim 1''$, prevents a very detailed comparison).

The hourglass structure emanating from the dense inner torus is clearly seen in both the optical and NIR continuum color images, Figs. 2 and 3. If we assume that the observed images are due to primary scattering, the intensity is proportional to the emission of the central star multiplied by $(1 - e^{-\tau_s}) \times e^{-\tau_e}$, where τ_s is the scattering optical depth at the observed region and τ_e is the extinction (absorption plus scattering) optical depth in the path from the star to the scattering material (and eventually from it to the observer). Since the extinction is expected to increase with the frequency, the scattered light becomes very red when $\tau_e \gg 1$. In the presence of an hourglass-like geometry, τ_e must be higher for higher polar angles; if, moreover, the extinction is very high close to the star (as we have deduced above), one expects the lobe walls to be prominent in the color images.

For larger distances from the equator and in both directions, a filamentary and clumpy structure (closely associated with the axis) becomes dominant in the continuum images and, in fact, carries most of the mass. We know, from the CO data (Sect. 4, Alcolea et al. 2001), that all these components are outflowing with a velocity roughly proportional to the distance to the star and that the average densities in them are $\sim 10^4$–10^5 cm^{-3}.

In summary, the close surroundings of the star are dominated by a torus-like structure with densities as high as 10^7 cm^{-3}, which continues out of the equator forming an hourglass-like structure. (In our summary of the nebular component properties, Fig. 4, see also Sect. 4, the inner components are labeled as feature H.) From about $5''$, however, filamentary clumps tightly distributed along the axis become the dominant nebular component, in the sense that they are bright in optical continuum and also that they represent most of the mass at these distances; the densities are still high but about 100 times lower than in the central torus. Slightly farther from the equator, weak Hα emission appears.

It is important to note that also in the central regions there are signs of shocks, as we can infer from the anomalously intense HCO^+ emission, even if the Hα emission is very weak. As we see in Sánchez Contreras et al. (2000b) there are two clear HCO^+ maxima in the central nebula, placed at about $3''$ from the star (but not exactly on the symmetry axis). A more detailed inspection of the spatial distribution and velocity of the HCO^+ line emission shows that the central star is surrounded by a wide expanding shell of shocked material, with a typical diameter $\sim 1.2 \times 10^{17}$ cm (equivalent to $5''$–$6''$) and expansion velocity ~ 40 km s^{-1}. Inside such a shell, HCO^+ is very weak and there is no indication of recent shocks. The only counterpart of this feature in our images would be the high-obscuration torus (and nearby hourglass structure), in which, we propose, the shock detected by means of the HCO^+ emission would be propagating. The existence of this shocked shell would imply that the star continued to eject very fast material (that is now interacting with the surrounding dense nebula) significantly after the acceleration of the dense molecular gas that forms the elongated, dense structures (that took place about 800 yr ago, see Sect. 1).

3.4. Spatial distribution of the scattered light intensity

In this section, we analyze the scattered light distribution seen in the broad-band continuum images, with focus on the optical images. A complete, combined analysis of the optical and near-IR scattered light is deferred to another paper (Sahai et al. 2002), since detailed modeling (including multiple scattering) is required for studying the optically thick regions of the nebula, and for estimating the mass of dust in various parts of the nebula. The very red $H - K$ colors seen in the central nebular region as well as the lower-latitude regions of the hourglass shaped lobes (black, orange and red regions in the $H - K$ color image) clearly indicate that the light reaching these regions suffers heavy radial extinction (see Sect. 3.3), and the scattering optical depths may also be large. Only the nebular regions lying along and near the nebular axis have an $H - K$ color which is roughly similar to that expected from the intrinsic starlight due to a M9III star. A much larger fraction of the southern lobe, compared to the northern one, shows such relatively blue $H - K$ colors. In the axial regions of this lobe, the ratio of the 2.05 to 1.6 μm wavelength-specific intensity, R_{KH}(obs), lies in the range 0.62–0.70, as compared to the intrinsic ratio, $R_{KH}(0)$, of 0.66 (assuming $T_{eff} = 2500$ K). Since the wavelength-dependent scattering results in bluing of the intrinsic starlight, whereas extinction produces reddening, the similarity between R_{KH}(obs) and $R_{KH}(0)$ implies that there is significant extinction of starlight between the central star and these regions. This extinction is most likely produced in the central regions, since the $H - K$ color remains fairly constant beyond a radius of about $2''$ in the axial regions, thus the corresponding optical depth, τ_e, does not vary radially in these regions. Using Eq. (1) of Sahai et al. (1999) for the observed scattered light intensity at any point in the nebula (setting $y = 1$), we derive $\tau_e = 1.37$ at 2.05 μm from $R_{KH}(\text{obs})/R_{KH}(0)$. We have assumed specific dust properties (i.e. the wavelength dependent extinction and albedo) from the tabulation by Whitney (1988). A similar exercise

using the observed ratio of the 0.79 to the 2.05 μm intensities (about 0.12), gives $\tau_e = 1.39$ at 2.05 μm. The corresponding 0.79 μm extinction is then 7.3 which compares very well with the value (7.4) inferred from applying Eq. (1) of Sahai et al. (1999) to the ratio of the 0.79 μm and 2.05 μm intensities.

Focusing our attention on the southern lobe and the F791W image, we find that the average surface brightness of the faint distant clumps near/along the axis varies in a very peculiar and unexpected manner with radius – it does not show a strong decrease with the distance to the star, R. For example, the average F791W intensities in 1×1 arcsec^2 regions at angular distances of 20.5, 22.6, 26.0, 28.4, 32.5, and 37.2 arcsec are 1.9, 1.4, 2.6, 1.8, 1.9, and 2.3×10^{-20} erg cm^{-2} s^{-1} Å^{-1} arcsec^{-2}. (The signal-to-noise ratio in the F675W image is much too low in these distant regions for it to be useful in this analysis.) In contrast, a strong radial decrease is expected as a product of two contributions (a) the R^{-2} decrease in the intensity of the illuminating starlight and (b) a decrease in the scattering optical depth because of a radial decrease in density as inferred from CO observations (e.g. for a spherical envelope with a $R^{-\alpha}$ decrease in density, the scattering optical depth would decrease as $R^{1-\alpha}$). In item (a) above, we are assuming that most of the radial extinction is produced close to the central source; however, if there is significant radial extinction near and in the scattering regions, it will contribute to an even faster (than R^{-2}) decrease of the starlight incident on the dust in the scattering regions for item (a) above. We note however that, since we derive 0.79 μm scattering optical depths in these southernmost clumps $\gtrsim$1, the variation of their mass found from CO data is not expected to have a strong effect on the scattered light intensity.

There are two possible explanations for the peculiar radial variation of the F791W intensity in the axial clumps of the southern lobe. The first explanation is that some of the field stars seen within the southern lobe are located physically close to specific clumps and increase their illumination. We assess the importance of such illumination by estimating the *maximum* surface brightness of an axial dust clump, $S_{\rm fld}$, produced by the *brightest* of the three prominent field stars which are seen in projection within the southern lobe. We find that $S_{\rm fld}$(0.79 μm) is 25% of the observed surface brightness of the dust clump near the star located 33.9 arcsec from the nebular center. We have made the most optimistic assumptions for this estimate – namely, that the projected separation between the star and the clump is equal to the actual separation, that there is no attenuation of the light reaching the dust and that all of it is scattered. Since the illumination decreases with the square of the distance between the clump and the star, and because larger clump scattering optical depths also lead to a larger fraction of the light being absorbed within the clump, our estimated $S_{\rm fld}$ is likely to be overestimated by a factor $\gtrsim$4. A strongly-peaked forward or backward-scattering phase function is also unlikely to increase $S_{\rm fld}$, because of the corresponding increase in the actual separation of the star and clump for scattering angles close to 0° or 180°. We therefore conclude that the illumination of dust by field stars is unlikely to be the cause of the peculiar radial variation of the F791W intensity in the axial clumps. The second explanation is that the clumps are being illuminated by starlight which varies as a function of the line-of-sight from the star to the scattering regions due to variable extinction close to the star, resulting in preferential illumination of specific clumps. This is not unlikely, given the large amount of radial extinction at 0.79 μm in the central regions of the nebula.

4. Physical conditions and kinematics of the different components of OH 231.8+4.2

In the previous section, we have distinguished a number components in OH 231.8+4.2, which are schematically shown in Fig. 4. Features A to E (Fig. 4, left panel) correspond to high-excitation gas emitting in Hα. Features F to J (right panel) describe low-excitation gas only detected by means of molecular emission or scattered light images.

In order to get a more quantitative description of the hot components of the nebula, we have performed estimations of their density and mass from our Hα images. For that we have used the well known relation between the Hα intensity integrated over a sky area and the corresponding "emission measure":

$$M(M_\odot) = 1.7 \times 10^{12} F(\mathrm{H}\alpha)/n. \quad (1)$$

Where $M(M_\odot)$ is the mass of the emitting region in solar masses, F(Hα) is the integrated Hα emission (erg cm^{-2} s^{-1}), and n(cm^{-3}) is the typical density (i.e. the electron density, that we will assume to be similar to the H density). This equation holds for ionized-H gas (HII regions) with kinetic energy, $T_{\rm k} = 10\,000$ K, He/H fractional abundance equal to 0.1 and assuming a distance D = 1500 pc. These are the expected conditions for the Hα emitting gas in OH231.8+4.2. Note that the proportionality coefficient varies with D^2, but is only weakly dependent on the gas temperature.

The combination of Eq. (1) with the geometric relation between mass, volume V(cm^3) and density, $M(M_\odot) = 1.2 \times 10^{-57}\ V\ n$, yields:

$$n = 3.8 \times 10^{34} \sqrt{F(\mathrm{H}\alpha)/V} \quad (2)$$

and

$$M(M_\odot) = 4.5 \times 10^{-23} \sqrt{F(\mathrm{H}\alpha)\ V}. \quad (3)$$

So, both density and total mass can be determined in this way for the different nebular components. We note that, to be reliable, this method requires a relatively good knowledge on the emitting volume. Our accurate images can provide such data, with the additional, reasonable assumption of cylindrical symmetry. In Fig. 4, left panel, we have shown the regions of the Hα brightness distribution assigned to each of these components.

Table 1. Physical conditions in the different components identified in our images.

feature (Fig. 4)	T_k (K)	mass ($M_\odot$)	volume ($10^{17\times3}$cm^3)	density cm^{-3}	axial velocity (km s^{-1})	tang. velocity (km s^{-1})	comments
A	$\sim10^4$	1.2×10^{-4}	1.0	100	150	negl.	northern forward shock
B_1	$\sim10^4$	5.3×10^{-4}	3.9	110	$\sim$150	$\sim$50	northern reverse shock
B_2	$\sim10^4$	6.3×10^{-5}	0.21	250	110	$\sim$50	northern reverse shock (bright ridge)
C_1	$\sim10^4$	$\sim3.5\times10^{-4}$	$\sim$6.6	45	$\sim$120	$\sim$100	southern shocked bubble (outer-east)
C_2	$\sim10^4$	$\sim2.4\times10^{-4}$	$\sim$4.4	45	$\sim$120	$\sim$100	southern shocked bubble (outer-west)
C_3	$\sim10^4$	$\sim1.7\times10^{-4}$	$\sim$3.4	40	$\sim$30	$\sim$40	southern shocked bubble (inner-east)
C_4	$\sim10^4$	$\sim1.4\times10^{-4}$	$\sim$3.0	40	$\sim$30	$\sim$40	southern shocked bubble (inner-west)
D	$\sim10^4$	7.3×10^{-5}	1.1	55	400	negl.	southern forward shock
E_1	$\sim10^4$	5.2×10^{-4}	8.9	50	330	$\sim$40	southern reverse shock
E_2	$\sim10^4$	6.0×10^{-5}	.96	50	160	negl.	southern reverse shock (inner feature)
F	25	0.05	0.2	1.8×10^5	150	negl.	northernmost dense clumps
G	15	0.1	0.5	1.3×10^5	40–110	negl.	northern collimated flow
H	35	0.64	0.2	3×10^6	$\sim$20	$\sim$20	central dense region (torus+hourglass)
I_1	25	0.1	0.5	1.3×10^5	40–200	negl.	southern collimated tail (inner)
I_2	10	0.035	0.5	2–9 $\times10^4$	200–340	negl.	southern collimated tail (outer)
J	8	0.001	0.2	$\sim4\times10^3$	400	negl.	southernmost axial clumps

Only in component C, the inflated shocked bubble in the southern lobe (Fig. 4), it is necessary an uncertain assumption about the total extent of the bubble, since only the emission from the bubble boundaries is well detected. We will assume that the bubble is complete and defined by a typical width/radius ratio $\sim$0.1. The densities and total masses of the outer (C_1 and C_2 in Fig. 4) and inner (C_3, C_4) regions and of the east and west hemispheres are calculated separately. We must keep in mind that in this case the calculations are particularly uncertain.

The average densities and total masses of the different components in which the Hα nebula has been divided (Fig. 4) have been calculated in this way and are given in Table 1. We have taken into account the moderate effects of extinction in the optical calculated by Sánchez Contreras et al. (2000a).

Our calculations yield mass values about twice as large as those found by Sánchez Contreras et al. (2000a); our densities are in general smaller, by a factor ranging between approximately 1 and 10. Both results, however, are not incompatible, given the different reach and accuracy of both methods. Sánchez Contreras et al. estimated the densities from the SII 6700 Å line ratio; SII and Hα data were used to estimate the emitting volume and so the total mass (we have checked that the Hα intensities given in this paper are in agreement with those from Sánchez Contreras et al.). Those calculations were quite uncertain since the density determination strongly depends on the relative intensity of the SII lines, which were quite noisy, and since these lines were only detected in a few clumps. So, probably the high densities measured with that method only apply to compact regions with very high density, which would dominate the very restricted SII emission. The estimation of the mass from the method by Sánchez Contreras et al. tends to select the regions emitting in SII lines, probably occupying a too small volume, and also yielding relatively low mass values. Our method uses the widespread Hα emission (which is expected to be a good tracer of HII regions) and is only moderately model dependent, note in particular the slight dependence on the assumed volume and temperature. Therefore, our results are a better estimation of the density and mass of the extended features detected in Hα emission, which are probably very similar to the total region ionized by the shocks.

In Table 1 we also reproduce the estimations of the temperature, density and mass of the different components of the dense, collimated outflow, measured by means of CO line emission (from Alcolea et al. 2001, see distribution of these components in Fig. 4).

Finally, we have listed in Table 1 axial and tangential velocities deduced from the CO and long-slit data (Alcolea et al. 2001; Sánchez Contreras et al. 2000a), in order to compare the linear momentum and kinetic energy carried by the different nebular components. Sometimes these velocities are uncertain, since the interpretation of spectroscopic data and *HST* imaging simultaneously is very complex (we plan to develop a spatiokinematical nebular model explaining all existing information in a forthcoming paper, Alcolea et al. 2002).

The first conclusion from these estimations of the mass, volume and density is that the clumps composing the collimated cold flow are significantly more compact, dense and massive than the components of the hot shocked gas emitting in Hα (as it was already expected

from previous data, Sects. 1, 3). For this reason, the momentum and energy carried by these dense components are about two orders of magnitude larger than that of the hot shocked gas. If we accept, from our discussion in Sect. 3, that the Hα emitting gas has been shocked by the collimated flow, we understand that the kinematics and temperature of such a very massive impinging jet is only slightly affected by the wind interaction process, while the opposite holds for the Hα emitting gas, as we indeed deduced from its properties.

The shocked hot gas shows a remarkable constant density; in the southern lobe (features C, D, E; Fig. 4, Table 1), for instance, the estimated density varies between 40 and 55 cm^{-3}; in the northern forward shock the density is $\sim$100 cm^{-3}. This result is in agreement with hydrodynamical calculations (Stone & Norman 1993a,b; Raga et al. 1995; Frank & Mellema 1996), which in general predict a significantly constant density along the forward shock, including both the head of the bow shock and the lateral inflated walls. Only in the northern very intense ridge (feature B_2) the density may exceed 200 cm^{-3}. We stress that the masses of the northern and southern Hα features (excluded the uncertain mass of the inflated southern lobe, feature C, which has no counterpart in the northern Hα lobe) are equal within a 10%, which is a very good agreement in view of the uncertainties and the very different extents. We recall that a similar result is found for the dense northern and southern collimated flows (Alcolea et al. 2001, Table 1).

5. Conclusions

We present high-resolution *HST* images of the protoplanetary bipolar nebula OH 231.8+4.2 in Hα and NII line emission and in scattered light in the continuum at 6750 and 7910 Å. We also discuss NICMOS images of scattered light in the NIR, from the *HST* archive, as well as previously published observations of CO line emission (Alcolea et al. 2001) and in long-slit optical spectroscopy (Sánchez Contreras et al. 2000a). The data are presented in Figs. 1–3.

We argue that the optical line images identify relatively hot and diffuse shocked gas. Meanwhile, the scattered and CO data probe denser and cooler gas, tightly associated with the nebula axis of symmetry. Both components flow from the nebula center at velocities as high as 400 km s^{-1}; the velocity of the collimated dense component is mainly axial, whereas the hot gas velocity also shows a significant tangential component. Both gas components have probably been accelerated by shocks. The dense component was first accelerated by a strongly radiative shock, became elongated and entered in interaction with more diffuse, outer shells. The shocks propagating in them became adiabatic and strong Hα emitters when their density (and cooling rate) was sufficiently low. This interpretation and the density calculations for the different components (see below) are compatible with our previous discussion on the change from radiative to adiabatic shocks (Sánchez Contreras et al. 2000a).

We have been able to distinguish a number components in the nebula, which are schematically shown in Fig. 4. In the northern lobe (Sect. 3.1), the shocked (Hα emitting) component is composed of a forward shock, feature A in Fig. 4, and a terminal jet shock (the outermost backward or reverse shock, associated with the Mach disk), feature B_2 and its extension B_1. The forward shock runs in a diffuse shell, while the backward shock runs in (we think) relatively diffuse gas associated with the impinging jet or flow. The densest parts of the impinging jet, which releases the energy and momentum necessary to form the shocks, correspond to the axial component detected in scattered light and CO emission (features F and G in Fig. 4). However, this dense axial flow is distinct from the Hα and NII emitting gas; we argue that this is because the very high excitation needed to power this optical line emission can only be present in the shock components running in relatively diffuse gas. However, we have found other shock signs in the dense axial flow, close to the reverse shock region: changes in the flow structure and dynamics and the presence of some shock-induced chemistry, like a high HCO^+ abundance (Sánchez Contreras et al. 2000b). Therefore, we conclude that there are also (backward) shocks propagating in this very dense component.

Our scattered light images also identify a low-excitation cavity in the northern lobe, surrounding the axial flow and extending axially up to the Hα emitting shocks. This cavity has been probably formed by gas expelled outwards from the axis by the shock passage.

In the southern lobe (Sect. 3.2), we can identify similar components. In this case, we find a double shocked bubble: a wide component (feature C in Fig. 4) and a bow shock (feature D). In the intersection of both "domes" there is a bright line emission region, feature E. We think that this component is associated with the terminal jet shock, though in this case the arguments are less strong than for the northern lobe. Again, the dense southern "tail" detected in scattered light (features I, J) seems to be the axial jet that produces the shocks, after impinging on a relatively diffuse and slow shell. No Hα emission is found in this dense flow, but its geometry and kinematics also suggests the presence of reverse shocks in it.

The central part of the nebula (Sect. 3.3), probed by our continuum images but not detected in optical line emission, is composed of a high-obscuration and very dense disk or torus plus a kind of hourglass-like structure that emanates from the disk (feature H en Fig. 4). The central (red) star of OH231.8+4.2 cannot be directly detected in the optical or NIR, due to the high obscuration of the nebula center, but is identified from SiO maser emission (Sánchez Contreras et al. 2000b). The comparison of interferometric mm-wave data and our images shows that the star lies in the center of the dense disk. The hourglass structure reveals that the gas regions adjacent to the disk, at distances smaller than about 5″ from the equator, form

two open cavities. Farther out, the filamentary flow mentioned above carries most of the gas.

Also in these central regions, we find signs of recent shock activity (even if Hα is not detected), mainly from the presence of intense HCO^+ emission. We think that shocks are in particular affecting (some parts of) the central dense ring.

We have finally estimated the mass, density and momentum of the different components identified from our optical line imaging (features A to E, Fig. 4, left panel). Similar parameters have been taken from CO data by Alcolea et al. (2001) for the cool components (features F to J, Fig. 4, right panel). The methods are described in Sect. 4 and the results are summarized in Table 1, where estimations of the temperature and emitting volume are also given. We confirm that the collimated cool component is significantly more compact, dense and massive than the components of the hot shocked gas emitting in Hα. The momentum and energy carried by these dense components are about two orders of magnitude larger than that of the hot shocked gas. The difference in the total mass is still larger, since the mass of the cool components is $\sim$1 $M_\odot$, while that of the hot, Hα-emitting gas is just $\sim 2\times10^{-3}$ $M_\odot$.

If the hot gas bubbles are the result of shock interaction between the collimated flow and more diffuse, outer shells, as we have suggested above, it is easy to understand that the kinematics and temperature of such a very massive impinging jet is only slightly affected by the wind interaction process. The opposite holds, however, for the diffuse Hα emitting gas, which has been heated and accelerated by a strong shock propagating at more than 400 km s^{-1}.

We have discussed in Sect. 3 the comparison of our results with existing hydrodynamical models of shock interaction (Raga et al. 1995; Frank & Mellema 1996, etc.). In general we conclude that our results, i.e. our images and the above interpretation of the shock structure, are compatible with the model predictions. However, this comparison is only qualitative, since no model is well adapted to the case we are discussing. We hope that the present detailed and quantitative description of the different components of the shock interaction in a PPN, including high-resolution images and mass and density estimations, will motivate new calculations and allow a quantitative comparison of theoretical predictions and empirical data. A comparison that seems necessary to improve present models and, therefore, for a better understanding of the dynamical processes involved in PN shaping.

Acknowledgements. This work has been supported by the Spanish DGESIC and PNIE, under grants AYA2000-0927 and 1FD97-1442. R.S. has been supported by NASA through (1) grant HST-GO-08326.01-A from the Space Telescope Science Institute (operated by the Association of Universities for Research in Astronomy, Inc., under NASA contract NAS5-26555), and (2) LTSA grant 399-20-61-00-00.

References

Alcolea, J., Bujarrabal, V., Sánchez Contreras, C., Neri, R., & Zweigle, J. 2001, A&A, 373, 932
Alcolea, J., et al. 2002, A&A, in preparation
Bowers, P. F., & Morris, M. 1984, ApJ, 276, 646
Bieging, J. H., Meakin, C. A., Kelly, D. M., et al. 2000, in Asymmetrical Planetary Nebulae II: From Origins to Microstructures, ed. J. H. Kastner, N. Soker, & S. Rappaport, ASP Conf. Ser., 199, 183
Cohen, M. 1981, PASP, 93, 288
Cohen, M., Dopita, M. A., Schwartz, R. D., & Tielens, A. G. G. M. 1985, ApJ, 297, 702
Frank, A., & Mellema, G. 1996, ApJ, 472, 684
Hartigan, P., Raymond, J., & Hartmann, L. 1987, ApJ, 316, 323
Hartigan, P. 1989, ApJ, 339, 987
Jura, M., & Morris, M. 1985, ApJ, 292, 487
Kastner, J. H., Weintraub, D. A., Zuckerman, B., et al. 1992, ApJ, 398, 552
Kastner, J. H., Weintraub, D. A., Merrill, K. M., & Gatley, I. 1998, AJ, 116, 1412
Mellema, G., & Frank, A. 1997, MNRAS, 292, 795
Raga, A. C., Taylor, S. D., Cabrit, S., & Biro, S. 1995, A&A, 296, 833
Reipurth, B. 1987, Nature, 325, (6107) 787
Sahai, R., Zijlstra, A., Bujarrabal, V., & te Lintel Hekkert, P. 1999, AJ, 117, 1408
Sahai, R., et al. 2002, A&A, in preparation
Sánchez Contreras, C., Bujarrabal, V., Miranda, L. F., & Fernández-Figueroa, M. J. 2000a, A&A, 355, 1103
Sánchez Contreras, C., Bujarrabal, V., Neri, R., & Alcolea, J. 2000b, A&A, 357, 651
Sánchez Contreras, C., Desmurs, J. F., Bujarrabal, V., Alcolea, J., & Colomer, F. 2002, A&A, 385, L1
Stone, J. M., & Norman, M. L. 1993a, ApJ, 413, 198
Stone, J. M., & Norman, M. L. 1993b, ApJ, 413, 210
Whitney, B. A. 1988, Rev. Mex. Astron. Astrofis. (Ser. Conf.) 1, 201